

On Polarization Dependent Equalization in 5G mmWave Systems

Farah Arabian ¹ and Michael Rice ²

¹Brigham Young University

²Affiliation not available

December 9, 2023

Abstract

The outputs of a cross-polarized antenna can produce a pair of different parallel frequency-selective channels. The optimum combining strategy is derived from maximum likelihood principles and used to define an equivalent discrete-time model. The simulated post-equalizer BER results show that optimum combining produces the best results, selection diversity can provide reasonably good results, and that both optimum combining and selection diversity can be superior to linear equalizer operating on the

channel obtained by combining the antenna outputs before applying a channel matched filter.

On Polarization Dependent Equalization in 5G mmWave Systems

Farah Arabian, Gregory P. Nordin, and Michael Rice
 Department of Electrical & Computer Engineering
 Brigham Young University, Provo, Utah, USA
 Email: farah.arabian@gmail.com, nordin@byu.edu, mdr@byu.edu

Abstract—The outputs of a cross-polarized antenna can produce a pair of different parallel frequency-selective channels. The optimum combining strategy is derived from maximum likelihood principles and used to define an equivalent discrete-time model. The simulated post-equalizer BER results show that optimum combining produces the best results, selection diversity can provide reasonably good results, and that both optimum combining and selection diversity can be superior to linear equalizer operating on the channel obtained by combining the antenna outputs before applying a channel matched filter.

I. INTRODUCTION

Smartphones have played a vital role in worldwide growth in data rates during the last decade. The data requirement for applications such as multimedia gaming, augmented reality and virtual reality demand higher data rate for better users experiences. 5G provides higher data rates compared to the previous technologies such as LTE (4G), UMTS (3G) and GSM (2G). The bandwidth required for these higher data rates may be obtained by exploiting the large bandwidths available in the millimeter wave (mmWave) band [1]. However, there are challenges associated with the mmWave band: poor propagation through structures, severe shadowing, and the need for line-of-sight propagation to achieve a good link.

Given the high data rates and correspondingly large bandwidths anticipated for 5G use in the mmWave band, multipath propagation will usually lead to frequency-selective fading. Furthermore, the current state of power amplifier circuit design makes it hard to deliver adequate power when a signal with a high peak-to-average power ratio (PAPR) is used. Consequently, single-carrier modulations, with lower PAPR than multicarrier modulations, are an attractive choice for this application [2].

A single-carrier modulation operating over a frequency-selective fading channel requires equalization. A smart phone equipped with one or more cross-polarized antennas produces a downlink comprising parallel frequency-selective channels. In this paper we show in Section II that the two parallel channels experienced by a cross-polarized antenna can be different, and this difference prompts the question of diversity combining. Motivated by this difference, we derive, based on maximum likelihood principles, the optimum combining strategy in Section III. In Section IV, we present a numerical examples that demonstrate the performance improvement using the optimum combining strategy and the penalties for using the incorrect combining strategy.

In this paper, boldface variables denote vectors or matrices with real-valued or complex-valued entries. The Hermitian (conjugate-transpose) operation is \mathbf{u}^H . The dot product for vectors \mathbf{u} and \mathbf{v} is denoted $\mathbf{u} \cdot \mathbf{v} = \mathbf{u}^H \mathbf{v}$ and the cross product is $\mathbf{u} \times \mathbf{v}$. The unit vectors in the x , y , and z directions are denoted \hat{x} , \hat{y} , and \hat{z} , respectively.

II. POLARIZATION-DEPENDENT MULTIPATH PROPAGATION

The complex-valued electric field corresponding to transverse wave propagation at position \mathbf{p} and at time t may be expressed as

$$\mathbf{E}(\mathbf{p}, t) = \mathbf{E}e^{j(\omega t - \mathbf{k} \cdot \mathbf{p})} \quad (1)$$

where $\mathbf{E} = E_x \hat{x} + E_y \hat{y} + E_z \hat{z}$ is a 3×1 vector denoting the (complex-valued) components of the electric field in the \hat{x} , \hat{y} , and \hat{z} directions; ω is the radian frequency (temporal period of the electric field); and $\mathbf{k} = k_x \hat{x} + k_y \hat{y} + k_z \hat{z}$ is the wave vector that defines the direction of propagation. The magnitude of \mathbf{k} , $k \equiv \|\mathbf{k}\|$ is the wave number and may be expressed as $k = 2\pi/\lambda = 2\pi f/v_p$ where λ is the wavelength, v_p is the propagation velocity, and f is the frequency in cycles/s. For the purposes of this paper, (1) is written as the product of three components:

$$\mathbf{E}(\mathbf{p}, t) = \mathbf{E}e^{-j\mathbf{k} \cdot \mathbf{p}} e^{j\omega t}. \quad (2)$$

The first term on the right-hand side of (2) quantifies the frequency-invariant magnitude, phase, and polarization state of the electric field. The second term on the right-hand side of (2) quantifies the frequency-dependent phase shift due to propagation delay. The third term on the right-hand side of (2) is the rotation operator. In the following, we are interested in the phasor terms $\mathbf{E}(\mathbf{p}) \equiv \mathbf{E}e^{-j\mathbf{k} \cdot \mathbf{p}}$.

A simple three-path propagation scenario corresponding to a downlink in an urban setting is illustrated in Figure 1. The antenna, located at point \mathbf{T} on the \hat{z} axis is the transmitter and a pedestrian with a hand-held smartphone is the receiver, designated point \mathbf{R} . In the coordinate system used here, the transmitter and receiver are confined to the $\hat{x} - \hat{z}$ plane. Line-of-sight propagation is assumed along the line \mathbf{TR} .

Multipath propagation occurs via two different paths: a ground reflection (at point \mathbf{G}) along the line segments \mathbf{TG} and \mathbf{GR} and a reflection off the side of a building (at point \mathbf{B}) along line segments \mathbf{TB} and \mathbf{BR} . The incidence angles

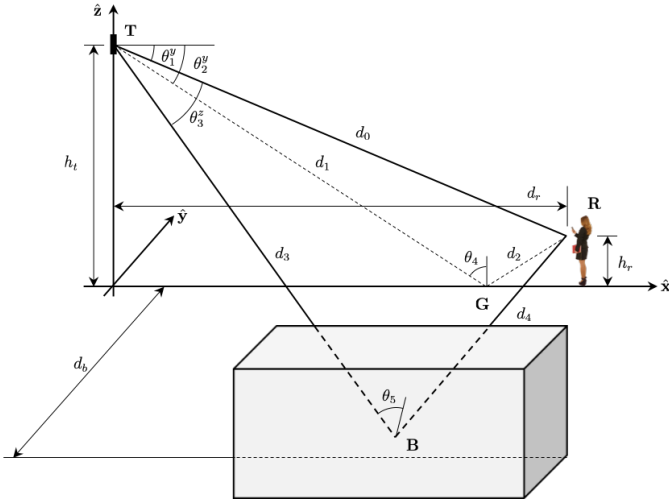


Fig. 1. Three-path radio propagation.

θ_4 and θ_5 are also shown in the figure. θ_4 is measured in the $\hat{x} - \hat{z}$ plane and θ_5 is measured in the **TBR** plane.

We are interested in the electric field components at point **R**, denoted \mathbf{E}_R . The electric field at **R** comprises three components, the electric field due to line-of-sight propagation $\mathbf{E}_{L,R}$, the electric field due to the ground reflection $\mathbf{E}_{G,R}$ and the electric field due to the reflection off the building $\mathbf{E}_{B,R}$:

$$\mathbf{E}_R = \mathbf{E}_{L,R} e^{-j2\pi f d_0/v_p} + \mathbf{E}_{G,R} e^{-j2\pi f (d_1+d_2)/v_p} + \mathbf{E}_{B,R} e^{-j2\pi f (d_3+d_4)/v_p}. \quad (3)$$

Assuming the transmit antenna is aligned with the \hat{z} axis, it can be shown, after considerable effort, that [3]

$$\mathbf{E}_{L,R} = \mathbf{R}_y(\theta_1^y) \mathbf{E}_0 e^{j\phi_L}; \quad (4)$$

$$\mathbf{E}_{G,R} = \mathbf{E}_{G,R}^{\text{TM}} + \mathbf{E}_{G,R}^{\text{TE}}, \quad (5)$$

where

$$\mathbf{E}_{G,R}^{\text{TM}} = r_{11} \begin{bmatrix} -\mathbf{E}_G^{\text{TM}} \hat{x} \\ \mathbf{E}_G^{\text{TM}} \hat{y} \\ \mathbf{E}_G^{\text{TM}} \hat{z} \end{bmatrix}, \quad (6)$$

$$\mathbf{E}_{G,R}^{\text{TE}} = r_{12} \begin{bmatrix} -\mathbf{E}_G^{\text{TE}} \hat{x} \\ \mathbf{E}_G^{\text{TE}} \hat{y} \\ \mathbf{E}_G^{\text{TE}} \hat{z} \end{bmatrix}, \quad (7)$$

with

$$\mathbf{E}_G^{\text{TM}} = \left[\mathbf{E}_G \cdot (\hat{\mathbf{n}}_1 \times \hat{\mathbf{k}}_1) \right] (\hat{\mathbf{n}}_1 \times \hat{\mathbf{k}}_1), \quad (8)$$

$$\mathbf{E}_G^{\text{TE}} = (\mathbf{E}_G \cdot \hat{\mathbf{n}}_1) \hat{\mathbf{n}}_1, \quad (9)$$

$$\mathbf{E}_G = \mathbf{R}_y(\theta_2^y) \mathbf{E}_0 e^{j\phi_G}; \quad (10)$$

$$\mathbf{E}_{B,R} = (\mathbf{E}_{B,R}^{\text{TM}} + \mathbf{E}_{B,R}^{\text{TE}}), \quad (11)$$

$$\mathbf{E}_{B,R}^{\text{TM}} = r_{22} \begin{bmatrix} -\mathbf{E}_B^{\text{TM}} \hat{x} \\ \mathbf{E}_B^{\text{TM}} \hat{y} \\ \mathbf{E}_B^{\text{TM}} \hat{z} \end{bmatrix}, \quad (12)$$

$$\mathbf{E}_{B,R}^{\text{TE}} = r_{21} \begin{bmatrix} -\mathbf{E}_B^{\text{TE}} \hat{x} \\ \mathbf{E}_B^{\text{TE}} \hat{y} \\ \mathbf{E}_B^{\text{TE}} \hat{z} \end{bmatrix}, \quad (13)$$

$$\mathbf{E}_B^{\text{TM}} = \left[\mathbf{E}_B \cdot (\hat{\mathbf{n}}_2 \times \hat{\mathbf{k}}_3) \right] (\hat{\mathbf{n}}_2 \times \hat{\mathbf{k}}_3), \quad (14)$$

$$\mathbf{E}_B^{\text{TE}} = (\mathbf{E}_B \cdot \hat{\mathbf{n}}_2) \hat{\mathbf{n}}_2, \quad (15)$$

$$\mathbf{E}_B = \mathbf{R}_z(\theta_3^z) \mathbf{R}_y(\theta_3^y) \mathbf{E}_0 e^{j\phi_B}, \quad (16)$$

where $\mathbf{R}_y(\theta)$ and $\mathbf{R}_z(\theta)$ are rotation matrices that perform rotations over the \hat{y} -axis and \hat{z} -axis, respectively;

$$\mathbf{E}_0 = [0 \ 0 \ 1]^T; \quad (17)$$

$\hat{\mathbf{k}}_1$ and $\hat{\mathbf{k}}_3$ are the unit vectors of **TG** and **TB**, respectively; $\hat{\mathbf{n}}_1$ and $\hat{\mathbf{n}}_2$ are the normal vectors for the planes **TGR** and **TBR**; ϕ_L , ϕ_G , ϕ_B are the initial phases in the **TR**, **TG** and **TB** directions; and θ_1^y , θ_2^y , θ_3^z , and θ_3^y are obtained from straight-forward geometry. The terms r_{11} , r_{12} , r_{21} , and r_{22} are TE-mode and TM-mode reflection coefficients for the planes **TGR** and **TBR**, respectively [3]; $n_1 = 1.000293$ is the refractive index of the propagation medium [air] and n_2 is the refractive index of the reflection surface. The following observations are of note:

- “ $1/R^2$ ” loss are not included in this analysis. The loss is simply a scale factor that impacts the signal-to-noise ratio, which is parameterized in the simulation results presented in Section IV.
- In (3), $\mathbf{E}_{L,R}$ and $\mathbf{E}_{G,R}$ only have \hat{x} and \hat{z} components. In contrast $\mathbf{E}_{B,R}$ has components in all three directions. The only contribution in \hat{y} is due to $\mathbf{E}_{B,R}$.
- If there were no reflection from the building, the electric field components in \hat{x} and \hat{z} would be scaled versions of each other. This is because all the interactions occur in the $\hat{x} - \hat{z}$ plane.
- The **TBR** propagation path contributes to the \hat{y} component. Consequently, the electric field components in the \hat{x} , \hat{y} , and \hat{z} directions can be *different*.

To illustrate the last point, we plot the electric field components in the \hat{x} , \hat{y} , and \hat{z} directions as a function of frequency for $h_t = 23$ m, $h_r = 1.15$ m, $d_r = 120$ m, and $d_b = 18$ m in a 500 MHz band centered at 28 GHz and assuming propagation through air ($v_p = c/n_1$) and concrete reflection surfaces: $n_2 = 2.2443 - j0.0597$ [4]. The result is

$$\begin{aligned} \mathbf{E}_R = & [0.1791 e^{-j2\pi f \tau_0} + (0.0671 + j0.0018) e^{-j2\pi f \tau_1} \\ & + (0.1326 - j0.0014) e^{-j2\pi f \tau_2}] \hat{x} \\ & + (0.0086 + j0.0005) e^{-j2\pi f \tau_2} \hat{y} \\ & + [0.9838 e^{-j2\pi f \tau_0} - (0.3336 + j0.0088) e^{-j2\pi f \tau_1} \\ & - (0.7426 - j0.0068) e^{-j2\pi f \tau_2}] \hat{z} \end{aligned} \quad (18)$$

where $\tau_0 = 406.58$ ns, $\tau_1 = 408.02$ ns, $\tau_2 = 423.92$ ns. The results are shown in Figure 2. The characteristic of interest is the difference between the electric fields in the \hat{x} , \hat{y} , and \hat{z} directions.

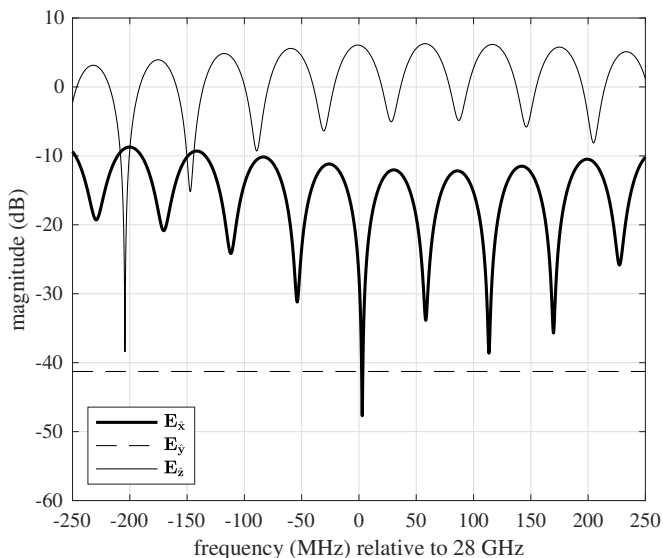


Fig. 2. A plot of the \hat{x} , \hat{y} , and \hat{z} components of (18) corresponding to the geometry shown in Figure 1 for $h_t = 23$ m, $h_r = 1.15$ m, $d_r = 120$ m, and $d_b = 18$, and $\phi_L = \phi_G = \phi_B = 0$.

Suppose the smartphone is positioned parallel to the $\hat{x} - \hat{z}$ plane in Figure 1 and is equipped with a cross-polarized antenna whose two antenna elements are aligned with \hat{x} and \hat{z} , respectively [5]. The multipath channel corrupting the downlink signal seen by the antenna element aligned with \hat{x} is *different* from the multipath channel corrupting the downlink signal seen by the antenna element aligned with \hat{z} .

In summary, a simple multipath scenario that takes into account the polarization state of the received wavefronts demonstrates that it is possible to experience different channels on the different polarizations. Even if different channels in the mmWave band are considered, the geometry is different but the conclusion is the same: it is possible for the different antenna elements to experience different channels. We now move to equalization and how the different channels should be combined to achieve a performance advantage.

III. EQUALIZATION WITH CROSS-POLARIZED ANTENNAS

To address the peak-to-average power ratio problem in the mmWave band, we assume single-carrier linear modulation is used to transmit p symbols. The complex-valued low-pass equivalent transmitted signal is of the form [6]

$$s(t) = \sum_{k=0}^{p-1} I_k g(t - kT_s) \quad (19)$$

where I_k is the k -th symbol drawn from a QAM alphabet of size M , T_s is the symbol time, and $g(t)$ is a unit energy pulse shape. This signal is transmitted from a linearly polarized antenna. The received signal is captured by a cross-polarized antenna that converts the electromagnetic wavefront corresponding to its two polarizations into two parallel waveforms. We assume the electronics that respond to the antenna element currents have identical noise figures and that their noise

contributions are independent. The parallel waveforms, $r_1(t)$ and $r_2(t)$, may be expressed as

$$r_1(t) = c_1(t) \star s(t) + z_1(t) \quad (20)$$

$$r_2(t) = c_2(t) \star s(t) + z_2(t) \quad (21)$$

where $c_1(t)$ and $c_2(t)$ are the complex-valued low-pass equivalent multipath channels representing the propagation in the two polarization states aligned with the receive antenna, \star is the continuous-time convolution operator, and $z_1(t)$ and $z_2(t)$ are uncorrelated complex-valued circularly symmetric Gaussian random processes each with autocorrelation function

$$E\{z_1(t + \tau)z_1^*(t)\} = E\{z_2(t + \tau)z_2^*(t)\} = 2N_0\delta(\tau). \quad (22)$$

Because $z_1(t)$ and $z_2(t)$ are uncorrelated, the joint density of $r_1(t)$ and $r_2(t)$ factors into the product of the marginal densities. Consequently, we may use, as the log-likelihood function

$$\Lambda(\mathbf{I}) = -\frac{1}{2N_0} \int_0^{(p-1)T_s} |r_1(t) - c_1(t) \star s(t)|^2 dt - \frac{1}{2N_0} \int_0^{(p-1)T_s} |r_2(t) - c_2(t) \star s(t)|^2 dt. \quad (23)$$

The signal portion of the log-likelihood function may be simplified using the following for $i = 1, 2$:

$$c_i(t) \star s(t) = \sum_{k=0}^{p-1} I_k \underbrace{c_i(t) \star g(t - kT_s)}_{h_i(t - kT_s)} \quad (24)$$

$$= \sum_{k=0}^{p-1} I_k h_i(t - kT_s). \quad (25)$$

Expanding the square and dropping terms that are not a function of the data symbols produces

$$\Lambda(\mathbf{I}) = \text{Re} \left\{ 2 \sum_{k=0}^{p-1} I_k^* y_1(kT_s) - \sum_{k=0}^{p-1} \sum_{k'=0}^{p-1} I_k^* I_{k'} x_1((k - k')T_s) \right\} + \text{Re} \left\{ 2 \sum_{k=0}^{p-1} I_k^* y_2(kT_s) - \sum_{k=0}^{p-1} \sum_{k'=0}^{p-1} I_k^* I_{k'} x_2((k - k')T_s) \right\} \quad (26)$$

$$= \text{Re} \left\{ 2 \sum_{k=0}^{p-1} I_k^* y(kT_s) - \sum_{k=0}^{p-1} \sum_{k'=0}^{p-1} I_k^* I_{k'} x((k - k')T_s) \right\} \quad (27)$$

where, for $i = 1, 2$,

$$y_i(kT_s) = \int r_i(t) h_i^*(t - kT_s) dt \quad (28)$$

$$x_i(mT_s) = \int h_i(t + mT_s) h_i^*(t) dt \quad (29)$$

and $y(kT_s) = y_1(kT_s) + y_2(kT_s)$ and $x(mT_s) = x_1(mT_s) + x_2(mT_s)$.

The maximum likelihood sequence is the sequence that maximizes (27). The observables are the channel-matched-filter outputs $y(kT_s)$. The matched filter outputs also define an equivalent discrete-time channel. Using (20), (21), and (25), the matched filter output may be expressed as

$$y(kT_s) = y_1(kT_s) + y_2(kT_s) \quad (30)$$

$$\begin{aligned} &= \sum_{n=0}^{p-1} I_n x_1((k-n)T_s) + \nu_1(kT_s) \\ &\quad + \sum_{n=0}^{p-1} I_n x_2((k-n)T_s) + \nu_2(kT_s) \end{aligned} \quad (31)$$

$$\begin{aligned} &= \sum_{n=0}^{p-1} I_n \underbrace{[x_1((k-n)T_s) + x_2((k-n)T_s)]}_{x((k-n)T_s)} \\ &\quad + \underbrace{\nu_1(kT_s) + \nu_2(kT_s)}_{\nu(kT_s)} \end{aligned} \quad (32)$$

$$= \sum_{n=0}^{p-1} I_n x((k-n)T_s) + \nu(kT_s) \quad (33)$$

where $\nu(kT_s)$ is a complex-valued proper Gaussian random variable with autocorrelation function

$$E\{\nu((k+m)T_s)\nu^*(kT_s)\} = 2N_0x(kT_s). \quad (34)$$

In most circumstances, the multipath channels $c_i(t)$ and the pulse shape $g_i(t)$ have finite support in t . Consequently, $x_1(mT_s)$, $x_2(mT_s)$, and $x(mT_s)$ have finite support in the discrete-time index m . Let L be such that $x_1(mT_s) = x_2(mT_s) = x(mT_s) = 0$ for $|m| > L$. Then, assuming $I_n = 0$ for $n < 0$ and $n \geq p$, (33) may be expressed as

$$y(kT_s) = \sum_{\ell=-L}^L x(\ell T_s) I_{k-\ell} + \nu(kT_s). \quad (35)$$

Equation (35) is the generalized Ungerboeck observation model [7] and is illustrated in Figure 3.

Using the symmetries of $x(nT_s)$, Ungerboeck showed that (27) may be simplified. For the case at hand, this simplification

$$\Lambda(\mathbf{I}) = \text{Re} \left\{ \sum_{n=0}^{p-1} I_n^* \left(2y(nT_s) - I_n x(0) - 2 \sum_{m=1}^L x(mT_s) I_{n-m} \right) \right\}. \quad (36)$$

Using (36), the well-known Viterbi Algorithm may be used to find the maximum likelihood sequence.

It is customary to whiten the Ungerboeck observation model. This is performed by performing the spectral factorization

$$X(z) = F(z)F^*(1/z^*) \quad (37)$$

where $F(z)$ is the z -domain polynomial formed from the zeros of $X(z)$ inside the unit circle. Using $1/F^*(1/z^*)$ as the noise

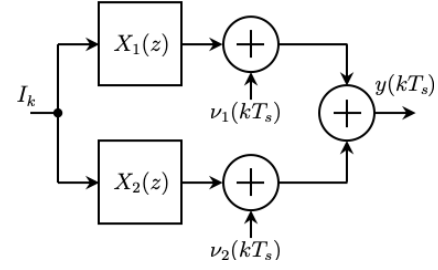


Fig. 3. Equivalent discrete-time model: the Ungerboeck observation model for optimum combining.

whitening filter produces the “whitened” equivalent discrete-time observation model

$$v(kT_s) = \sum_{\ell=0}^L f(\ell T_s) I_{k-\ell} + \eta(kT_s) \quad (38)$$

where $f(\ell T_s)$ is the inverse z -transform of $F(z)$ and $\eta(kT_s)$ comprises a sequence of complex-valued circularly symmetric Gaussian random variables with

$$E\{\eta(kT_s)\eta^*(mT_s)\} = 2N_0\delta_{k-m}. \quad (39)$$

Equation (38) is the Forney observation model [8].

The maximum likelihood sequence is the sequence that maximizes [8]

$$\Lambda'(\mathbf{I}) = \sum_{n=0}^{p-1} \left| v(nT_s) - \sum_{\ell=0}^L f(\ell T_s) I_{n-\ell} \right|^2. \quad (40)$$

The Viterbi algorithm may be used to find the sequence that minimizes (40).

In summary, maximum likelihood considerations define equivalent discrete-time channels that are generalizations of the Ungerboeck observation model. The equivalent discrete-time system defines equal-gain diversity combining operating on channel matched-filter outputs. That is, combining occurs *after* applying the parallel matched filters, not before.

IV. A NUMERICAL EXAMPLE

As an example, we use the \hat{x} and \hat{z} electric field components corresponding to the scenario used to produce Figure 2 as our two channels. The modulation is QPSK with a bit rate of 200 Mbits/s and using the square-root raised-cosine pulse shape with a roll-off factor of 0.5 and a span of 12 symbols [9].

The multipath channels were created using the following procedure. The channel impulse responses $c_1(t)$ and $c_2(t)$ are created by convolving the \hat{x} and \hat{z} components of (18) with the pulse shape, respectively. The channel matched filters were applied to $c_1(t)$ and $c_2(t)$ and sampled at 1 sample/symbol. Using the 99.99% total energy criterion, the Ungerboeck observation models are

$$X_i(z) = x_i(-3T_s)z^3 + \dots + x_i(0) + \dots + x_i(3T_s)z^{-3} \quad (41)$$

for $i = 1, 2$. The Ungerboeck observation model for the ML combined channel is $X(z) = X_1(z) + X_2(z)$. The Forney

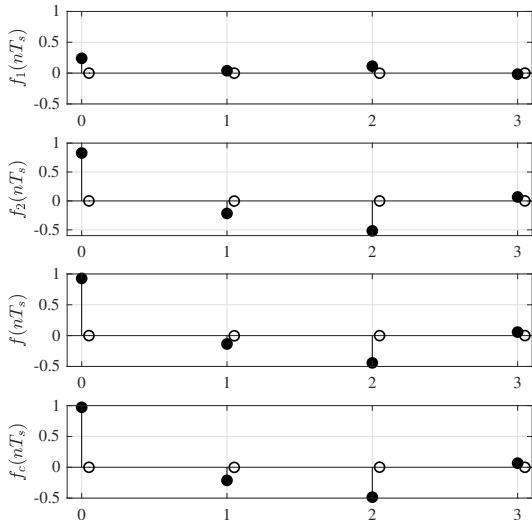


Fig. 4. The coefficients for the Forney observation model for the example of Section IV. The solid markers indicate the real parts of the coefficients, the clear markers the imaginary parts.

observation models based on the spectral factorizations of $X_1(z)$, $X_2(z)$, $X(z)$ and $X_c(z)$ are shown in top four plots in Figure 4. The coefficients shown in the bottom plot are derived from the channel that combines $c_1(t)$ and $c_2(t)$ before matched filtering and proceeds as outlined above to produce the Forney observation model denoted $F_c(z)$. This channel represents the case where equal-gain combining is applied to the antenna outputs.

The equalized bit error rate (BER) performance is assessed using linear minimum mean-squared error (MMSE) equalizer [6] operating on the samples $v(kT_s)$ defined (38). The MMSE equalizer filter is a length-31 FIR filter. In the simulations, the QPSK symbols are $I_k \in \{\pm A \pm jA\}$ and the signal-to-noise ratio is defined as A^2/N_0 . The channel $F(z)$ is scaled to that

$$\sum_{\ell=0}^L |f(\ell T_s)|^2 = 1. \quad (42)$$

The simulation results for the four channels in Figure 4 are plotted in Figure 5. The bit error rate (BER) performance of the ML combined channel [denoted $F(z)$ in the figure] is clearly better than the BER performance using the outputs of one of the antenna elements alone [$F_1(z)$ or $F_2(z)$ in the figure] and better than using the channel formed by combining the antenna outputs before matched filtering. The same result has also been observed in one different application [10].

V. CONCLUSION

This paper has examined the concept of data communication over parallel frequency-selective channels. Computing the electric fields in the three spatial dimensions for a simple geometry representing a dense urban setting shows that a cross polarized antenna produces parallel frequency-selective channels that can be *different*. Maximum likelihood (ML)

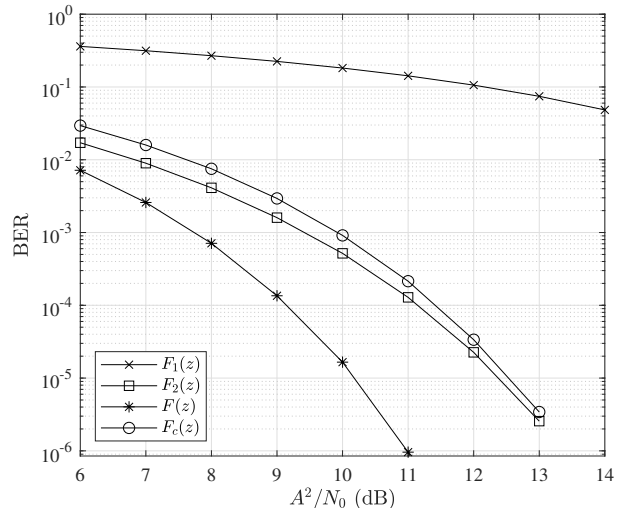


Fig. 5. BER simulation results.

analysis shows that the proper way to combine the parallel channels is to apply a filter matched to each channel then add the matched filter outputs. The equivalent discrete-time system for the case of different parallel channels was also derived and whitened. A linear MMSE equalizer was applied to the equivalent discrete-time model. The simulated post-equalizer BER results show that optimum combining produces the best results, selection diversity can provide reasonably good results, and that both optimum combining and selection diversity can be superior to the MMSE equalizer operating on the channel obtained by combining the antenna outputs before applying a channel matched filter.

REFERENCES

- [1] T. Rappaport *et al.*, "Millimeter wave mobile communications for 5G cellular: It will work!" *IEEE Access*, vol. 1, pp. 335–349, 2013.
- [2] S. Buzzi, C. D'Andrea, T. Foggi, A. Ugolini, and G. Colavolpe, "Single-carrier modulation versus OFDM for millimeter-wave wireless MIMO," *IEEE Access*, vol. 66, pp. 1335–1348, 2018.
- [3] C. Balanis, *Advanced Engineering Electromagnetics*. Hoboken, NJ: John Wiley & Sons, 1989.
- [4] M. Samimi and T. Rappaport, "Characterization of the 28 GHz Millimeter-Wave Dense Urban Channel for Future 5G Mobile Cellular," NYU Polytechnic School of Engineering, NYU Wireless TR 2014-001, 24 June 2014.
- [5] M.-Y. Li *et al.*, "Eight-port dual polarized MIMO antenna for 5G smartphone applications," in *IEEE Asia Pacific Conference on Antennas and Propagation*, Kaohsiung, Taiwan, 26–29 July 2016, pp. 195–196.
- [6] J. Proakis and M. Salehi, *Digital Communications*, 5th ed. New York: McGraw-Hill, 2007.
- [7] G. Ungerboeck, "Adaptive maximum-likelihood receiver for carrier-modulated data-transmission systems," *IEEE Transactions on Communications*, vol. 22, no. 5, pp. 624–636, May 1974.
- [8] G. D. Forney, "Maximum-likelihood sequence estimation of digital sequences in the presence of intersymbol interference," *IEEE Transactions on Information Theory*, vol. 8, no. 3, pp. 363–378, May 1972.
- [9] M. Rice, *Digital Communications: A Discrete-Time Approach*. amazon.com: Kindle Digital Publishing, 2018, ISBN-10: 1790588561. ISBN-13: 978-1790588565.
- [10] F. Arabian and M. Rice, "Polarization diversity and equalization of frequency selective channels in telemetry environment for 16APSK," in *Proceedings of the International Telemetry Conference 2019*, Las Vegas, NV, October 2019.